

# The Three Hundred Project hydrodynamical simulations: Hydrodynamical Weak-Lensing Cluster Mass Biases and Richnesses using different hydro models.

C. Giocoli<sup>1,2,\*</sup>, G. Despali<sup>3,1,2</sup>, M. Meneghetti<sup>1,2</sup>, E. Rasia<sup>4,5,6</sup>, L. Moscardini<sup>3,1,2</sup>, S. Borgani<sup>7,4,5,8,9</sup>, G. F. Lesci<sup>3,1</sup>,  
F. Marulli<sup>3,1,2</sup>, W. Cui<sup>10,11,12</sup>, G. Yepes<sup>10,11</sup>

<sup>1</sup> INAF-Osservatorio di Astrofisica e Scienza dello Spazio di Bologna, Via Piero Gobetti 93/3, 40129 Bologna, Italy

<sup>2</sup> INFN – Sezione di Bologna, viale Bertoni 6/2, I-40127 Bologna, Italy

<sup>3</sup> Dipartimento di Fisica e Astronomia "Augusto Righi", Alma Mater Studiorum Università di Bologna, via Gobetti 93/2, I-40129 Bologna, Italy

<sup>4</sup> INAF – Osservatorio Astronomico di Trieste, via Tiepolo 11, I-34131, Trieste, Italy

<sup>5</sup> IFPU, Institute for Fundamental Physics of the Universe, Via Beirut 2, 34014 Trieste, Italy

<sup>6</sup> Department of Physics; University of Michigan, Ann Arbor, MI 48109, USA

<sup>7</sup> Dipartimento di Fisica, Università di Trieste, Sez. di Astronomia, via Tiepolo 11, I-34131 Trieste, Italy

<sup>8</sup> ICSC - Italian Research Center on High Performance Computing, Big Data and Quantum Computing, via Magnanelli 2, 40033, Casalecchio di Reno, Italy

<sup>9</sup> INFN – Istituto Nazionale di Fisica Nucleare, Via Valerio 2, I-34127, Trieste, Italy

<sup>10</sup> Departamento de Física Teórica, Módulo 15, Facultad de Ciencias, Universidad Autónoma de Madrid, E-28049, Madrid, Spain

<sup>11</sup> Centro de Investigación Avanzada en Física Fundamental (CIAFF), Facultad de Ciencias, Universidad Autónoma de Madrid, E-28049, Madrid, Spain

<sup>12</sup> Institute for Astronomy, University of Edinburgh, Royal Observatory, Edinburgh EH9 3HJ, UK

Received *Space: 1999*; Accepted *2001: A Space Odyssey*

## ABSTRACT

**Context.** The mass of galaxy clusters derived from weak-lensing observations is sensitive to projection effects and, on average it is biased low with respect to the true cluster mass, with a mass and redshift dependence.

In this work, we leverage state-of-the-art hydrodynamical simulations of galaxy clusters, carried out with *GadgetX* and *GIZMO-SIMBA* as part of the Three Hundred Project. We use them to quantify weak-lensing mass biases with respect also to the results from dark matter-only simulations. We also investigate how the biases of the weak-lensing mass estimates propagate into the richness-mass relation.

**Aims.** Future wide-field weak-lensing surveys require per cent accuracy on the characterisation of cluster masses in order to use galaxy cluster number count and clustering as complementary probes for cosmological analyses. We aim to shed light on the effect of the presence of baryons on the weak-lensing mass bias and also whether this bias depends on the galaxy formation recipe; in addition, we seek to model the richness-mass relation that can be used as guidelines for observational experiments for cluster cosmology.

**Methods.** We produce weak-lensing simulations of random projections to model the expected excess surface mass density profile of clusters up to redshift  $z = 1$ . We adopt a Bayesian analysis to describe the weak-lensing cluster mass and concentration, as well as their associated posterior distributions.

**Results.** We derive the weak-lensing mass-richness relation and find consistency within  $1\sigma$  uncertainties across hydrodynamical simulations. The intercept parameter of the relation is independent of redshift but varies with the minimum of the stellar mass used to define the richness value. At the same time, the slope is described by a second-order polynomial in redshift, relatively constant up to  $z = 0.55$ . The scatter in observed richness at a fixed weak-lensing mass, or vice versa, increases linearly with redshift at a fixed stellar mass cut. Importantly, we observe that the scatter in richness at a given true mass is smaller than at a given weak-lensing mass. Our results align well with SDSS redMaPPer cluster observations when adopting a stellar mass cut of  $M_{\text{star, min}} = 10^{10} h^{-1} M_{\odot}$ . Finally, we present regression parameters for the true mass–observed richness relation and highlight their dependence on redshift and stellar mass cut, offering a framework for improving mass–observable relations essential for precision cluster cosmology.

**Key words.** dark matter – weak gravitational lensing – clusters of galaxies – hydrodynamical simulations

## 1. Introduction

Different wide-field observational facilities (Planck Collaboration 2016; Abbott et al. 2022; DESI Collaboration et al. 2024) and dedicated observations of galaxies and clusters (Bergamini et al. 2023; Diego et al. 2024) have highlighted that Dark Mat-

ter (DM) is the major matter component in our Universe. It is distributed along filamentary structures, walls, and nodes where clusters of galaxies are embedded (Malavasi et al. 2017; Libeskind et al. 2018; Santiago-Bautista et al. 2020; Feldbrugge & van de Weygaert 2024; Hoosain et al. 2024; Zhang et al. 2024).

Following the standard scenario of structure formation, cosmic structures form hierarchically and their average mass assem-

\* e-mail: carlo.giocoli@inaf.it

bly proceeds monotonically over time (Tormen 1998; Tormen et al. 1998; van den Bosch 2002; Wechsler et al. 2002; Giocoli et al. 2007). Galaxy clusters are the last virialised structures to form, DM dominates their mass content, while their central region is affected by different non-linear dynamic processes (Springel et al. 2001; Tormen et al. 2004) triggered by the baryonic physics (Cui et al. 2016; Arthur et al. 2017).

Baryons constitute the visible component of the clusters and can be observed in different wavelengths using facilities from the ground and space. In X-ray, clusters appear smooth since the X-ray photons are emitted via the Bremsstrahlung thermal emission of the diffuse and hot plasma, called intra-cluster medium. In the visible and near-infrared bands, instead, they look as a clumpy distribution of knots for the integrated emissions from individual stars in their hosting galaxies.

Due to their privileged role in the hierarchical structure formation scenario and their relatively easy detectability, clusters are an important cosmological probe (Bahcall et al. 1997; Costanzi et al. 2014; Planck Collaboration et al. 2014). Indeed, their mass distribution as a function of redshift, called the mass function, depends on several cosmological parameters that can be constrained once the observed function is compared with theoretical expectations derived from numerical simulations (Tinker et al. 2008; Despali et al. 2016; Euclid Collaboration: Castro et al. 2022).

The large amount of matter present in clusters makes them powerful gravitational lenses (Meneghetti et al. 2008, 2010b; Natarajan et al. 2024): they bend the light emitted by background sources located at much higher redshift. When light rays pass close to the cluster centre, the gravitational lensing regime is called ‘strong’: sources are highly magnified, distorted, and imaged multiple times. On the other side, far from the cluster centre, there is the ‘weak’ lensing case where background galaxies are only slightly distorted. In this situation, with the effect being tiny, it is necessary to average over a large number of galaxy image shapes to have a reliable estimate of the lensing signal from which one can derive a measure of the cluster potential and, thus, of the cluster mass. Leveraging on the advantage that gravitational lensing does not rely on any assumption on the dynamical state of the cluster, weak lensing is used in different wide-field cosmological surveys to weight cluster masses (Giocoli et al. 2024; Euclid Collaboration: Sereno et al. 2024; Euclid Collaboration: Ingoglia et al. 2024).

This approach provides an unbiased estimate of the projected matter density distribution (Bartelmann & Schneider 2001; Bartelmann 2010). Nevertheless, mostly due to projection effects, the recovered lensing mass is, on average, biased low with respect to the actual three-dimensional one (Meneghetti et al. 2008; Becker & Kravtsov 2011; Giocoli et al. 2012, 2014; Euclid Collaboration: Giocoli et al. 2024). Many dedicated works have been carried out based on state-of-the-art hydrodynamical simulations to assess the reliability of the recovered weak-lensing (hereafter also WL) mass (Grandis et al. 2019, 2021). However, one aspect that has so far received little attention is the quantification of the impact of baryonic physics on the reconstruction of the weak-lensing cluster mass as a function of redshift. Indeed, the collisional nature of the baryonic component, along with the processes related to radiative cooling, star formation and energy feedback from stars and AGN, all impact the distribution of baryons, thus back-reacting on the distribution of total mass (Rasia et al. in prep.). For instance, while cooling only triggers a sort of adiabatic contraction of halos (Gnedin et al. 2004), feedback from AGN has been shown to give rise instead to a slight adiabatic expansion. These processes combine to lead to an overall

different halo total matter distribution and cluster concentration, thereby affecting the lensing signal. At the same time, different numerical implementations of star formation in simulations can produce peaked sub-halos with higher and concentrated stellar distribution (Meneghetti et al. 2023; Li et al. 2023). In this way, sub-halos become more resistant to disruption within the cluster environment, with respect to a DM-only simulation (e.g. Dolag et al. 2009), thus increasing the normalization of the sub-halo mass function (Despali & Vegetti 2017; Ragagnin et al. 2022; Srivastava et al. 2024). Clearly, the amount, scale-dependence and time-scale over which such processes alter the total matter distribution in cluster-sized halos and in their substructures are determined by the details of the sub-resolution processes which ultimately determine galaxy formation in simulations. This investigation is essential for the exploitation of future wide-field surveys, which aim at accurate weak-lensing reconstruction of cluster masses to derive robust cosmological posteriors from cluster number counts. This is the first issue that we will tackle in this paper. We will compare the biases derived from three sets of simulations from the Three Hundred collaboration: one carried out with dark-matter particles only and the other two performed with different hydrodynamical codes and sub-grid modules. We would like to underline that it is beyond the scope of this study to quantify the effects due to shear bias, photometric redshift errors and cluster mis-centring. On the other hand, we will include the effect of contamination from nearby structures included within  $\pm 5$  Mpc along the line of sight with respect to the cluster centre.

The mass of individual systems derived from gravitational lensing is, as said, projected, and its three-dimensional reconstruction requires both high-quality data and, eventually, calibration using state-of-the-art dedicated numerical simulations (Euclid Collaboration: Ragagnin et al. 2024). This procedure can be applied to a limited number of objects with high signal-to-noise and cannot possibly be applied to the myriad of data that the aforementioned missions can provide. One way around is to utilize some mass proxies that are tightly correlated with the total mass. The approach can be extended to several mass proxies recovered from multi-band observations to provide well-calibrated mass-observable relations that can be used to estimate galaxy cluster masses for larger samples with known observable properties. As a first step, though, the same set of data that will be used for the lensing analysis (Ivezic et al. 2008, 2009; Laureijs et al. 2011) can be utilized to measure, as a mass proxy, the cluster richness, whose value is simply obtained by counting the number of satellite galaxies in a given aperture and above a given brightness limit or stellar mass.

This approach has already been used in the literature, e.g. by Costanzi et al. (2021) who jointly analysed redMaPPer galaxy clusters from the Dark Energy Survey (DES) Year 1 data and follow-up observations from the South Pole Telescope (SPT), calibrating the richness-mass relation. Their results show a consistency of the cosmological constraints with other probes when using a combined mass calibration. Adding high-redshift SPT clusters mildly improves the constraints. The characterization and calibration of the scaling relation between richness and WL mass critically depend on the photometric identification of background and foreground galaxies, as well as of the cluster members given a magnitude limit experiment. In addition, its parametrization hinges on the cluster sample selection function (Sartoris et al. 2016). Most prior studies forecasting cosmological constraints from galaxy cluster counts (e.g. Lima & Hu 2005; Sartoris et al. 2010; Carbone et al. 2012) have assumed a fixed precision for the parameters in the mass-observable scaling relationship rather than measuring or deriving it directly. Andreon

& Bergé (2012) developed a richness-mass scaling relation for a sample of X-ray selected galaxy clusters, showing that red sequence colour enables accurate redshift estimates. Using simulations, they also demonstrate that accounting for selection effects yields highly precise scaling parameters, improving cosmological forecasts from galaxy cluster data. Andreon (2016) provides a compilation of precise cluster masses using a calibrated richness-mass relation with a small scatter, enabling 0.16 dex mass accuracy, in principle superior to X-ray or SZ-based methods. The catalogue includes hundreds of clusters from the Sloan Digital Sky Survey and other catalogues, with careful determination of cluster centres, redshifts and line-of-sight contamination. The catalogue addresses comparison challenges between different mass catalogues, offering improved consistency for cluster mass measurements across various studies. In a more recent analysis, Lesci et al. (2022a,b) analyzed cluster counts in the AMICO KiDS-DR3 catalogue, jointly constraining cosmological parameters and the cluster mass-observable scaling relation using intrinsic richness as the observable linked to cluster mass. The sample includes thousands of clusters with large richness up to  $z = 0.6$ . Following Bellagamba et al. (2019) for the weak-lensing analysis, they corrected for incompleteness and impurities using a mock catalogue. Their model for cluster counts accounts for redshift uncertainties and incorporates the intrinsic scatter in the scaling relation, combining the likelihood functions to constrain both cluster counts and parameters, determining the mass-observable scaling relation.

Using the two hydro-simulation sets of The Three Hundred, the second goal of this work is to investigate the scaling relation between richness and mass obtained from WL data. In particular, we will focus on how the relation changes according to the stellar mass cut used to select the galaxy members and on the observational biases due to the weak-lensing mass calibration. Specifically, by using a mass-selected sample, we aim to set priors on the parameters defining the richness-mass relation, using cluster richness as our mass proxy. This analysis provides the necessary prior input for cosmological forecasts based on cluster counts and clustering.

The structure of this paper is as follows. In Section 2, we describe the simulations employed in this study and the methodology used to construct the weak-lensing signal from simulated clusters. Additionally, we present our findings on weak-lensing mass biases, examining their dependence on the hydrodynamical codes and their redshift evolution. In Section 3, we discuss the weak-lensing mass-observed richness relations – and its inverse, summarizing them into a final model and comparing our findings with existing results in the literature. In Section 4, we calibrate the scaling relation between true mass and observed richness. Finally, we summarize our main conclusions in Section 5.

All algorithms in this work are on base ten unless otherwise indicated.

## 2. Weak Lensing: the Simulations and the Model

### 2.1. The Three Hundred Project Runs

We build up our weak-lensing cluster images using simulated regions by the Three Hundred Collaboration (Cui et al. 2018, 2022). A total sample of 324 clusters has been mass-selected ( $M_{200} > 8 \times 10^{14} h^{-1} M_{\odot}$ ) at  $z = 0$  in the MultiDark MDPL2 cosmological N-Body simulation (Klypin et al. 2016). The original and resimulated runs have been performed assuming the cosmological parameters from the Planck Collaboration (2016)  $\Omega_m = 0.307$ ,  $\Omega_b = 0.048$ ,  $\Omega_{\Lambda} = 0.693$ ,  $h = 0.678$ ,  $\sigma_8 = 0.823$

and  $n_s = 0.96$ , following the evolution of  $3840^3$  collisionless particles with mass  $m_{\text{DM}} = 1.5 \times 10^9 h^{-1} M_{\odot}$  on a box with  $1 h^{-1}$  Gpc on a side. For each of the 324 regions – defined as being five times the virial radius of the cluster position on their centre, initial conditions with multiple levels of mass refinements were generated using the GINNINGAGAP code<sup>1</sup>, and dividing the mass content in baryonic and dark-matter mass according to the adopted cosmological baryon fraction, leading to:  $m_{\text{gas}} = 12.7 \times 10^8 h^{-1} M_{\odot}$  and  $m_{\text{dm}} = 2.36 \times 10^8 h^{-1} M_{\odot}$ , respectively. Starting from redshift  $z = 120$ , when the initial conditions have been generated, each zoom-in simulation has been run with two different hydro-solver algorithms: GadgetX (Rasia et al. 2015) and GIZMO-SIMBA (Davé et al. 2019; Cui et al. 2022). GadgetX simulations have been performed with a ‘modern’ smoothed-particle hydrodynamics (SPH) code based on Gadget-3 that includes artificial thermal diffusion, time-dependent artificial viscosity, high-order Wendland C4 interpolating kernel, and wake-up scheme (Beck et al. 2016). The GIZMO-SIMBA runs are completed with the GIZMO code (Hopkins 2015) with the state-of-the-art galaxy formation subgrid models following the SIMBA simulation (Davé et al. 2019). The Meshless Finite Mass (MFM) solver implemented in GIZMO evolves gas particles with a precise treatment of shocks and shear flows, eliminating the need for artificial viscosity. In addition, starting from the same initial conditions and setting exactly the same initial sampling of phase space, a collisionless DM-only run has been produced using Gadget-3. This run will be used as our reference.

These simulated regions have been previously used to investigate various properties of both the DM and the baryon content. Relevant to this paper, we mention the studies on the influence of the environment on galaxy properties (Wang et al. 2018), the cluster splashback radius characterization (Haggar et al. 2020; Knebe et al. 2020), the baryon profile (Li et al. 2023) and the hydrodynamical mass bias (Gianfagna et al. 2023), the strong lensing properties of the clusters (Vega-Ferrero et al. 2021) and their satellite galaxies (Meneghetti et al. 2023; Srivastava et al. 2024), and the weak-lensing mass bias (Euclid Collaboration: Giocoli et al. 2024).

At all the analyzed snapshots, nine from  $z = 0.12$  to  $z = 0.94$ , the main properties of each cluster are computed via the Amiga Halo Finder (Knollmann & Knebe 2009) and include the total mass  $M_{200}$ , defined as the mass within the radius  $R_{200}$  which encloses 200 times the critical density of the universe  $\rho_c(z)$  at the corresponding redshift,

$$M_{200} = \frac{4\pi}{3} R_{200}^3 200 \rho_c(z). \quad (1)$$

In particular, we define  $M_{200,\text{DM}}$  to be the cluster mass in the DM-only run.

As mentioned, to model the lens we also need the cluster concentration,  $c_{200}$  that adopting a Navarro-Frenk-White (hereafter NFW) density profile (Navarro et al. 1996, 1997) is defined as the ratio between  $R_{200}$  and the scale radius  $r_s$ , defined as the radius at which the logarithmic derivative of the density profile is equal to  $d \log \rho / d \log r = -2$ . Following the NFW density profile parametrisation, Prada et al. (2012) describe the halo concentration in terms of the velocity ratio as follows:

$$\frac{V_{\text{max}}}{V_{200}} = \sqrt{\frac{0.216 c_{200}}{\ln(1 + c_{200}) - c_{200}/(1 + c_{200})}}, \quad (2)$$

<sup>1</sup> <https://github.com/ginungagapgroup/ginungagap>

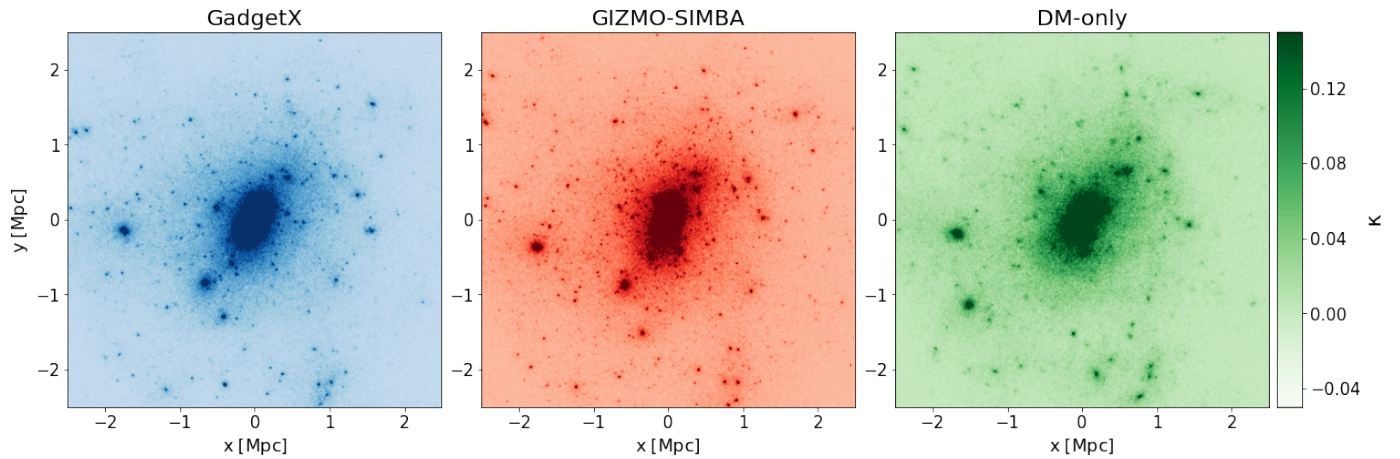


**Fig. 1.** Simulated convergence maps of a cluster lens – namely with ID=4 – at  $z_l = 0.22$  and considering  $z_s = 3$ , obtained collapsing the total mass along the  $z$ -projection. The left and the central panels show the results using two different hydro-solver GadgetX and GIZMO-SIMBA, respectively. In the right panel, we display the convergence map of the same cluster projection simulated using only collisionless dark matter particles, DM-only run. The assumed field of view is 5 Mpc by side, collapsing  $\pm 5$  Mpc matter along the line-of-sight.

where  $V_{200} = \sqrt{\frac{GM_{200}}{R_{200}}}$  represents the halo virial circular velocity and  $V_{\max}$  the maximum circular velocity. We derive  $c_{200}$  by solving numerically Eq. 2.

## 2.2. Cluster Weak-Lensing Simulations

To create and analyse the simulated lensing images, we follow the same procedure of *Euclid Collaboration: Giocoli et al. (2024)*, but here we extend the sample to both the GIZMO-SIMBA and the DM-only versions. For each of the 324 central clusters of the resimulated regions, we build three simulated excess surface mass density profiles, collapsing each time the particles into a single lens plane along the simulated box axes; this guarantees that the three projections are random with respect to the three-dimensional shape of the clusters. We repeat the same procedure for all nine different snapshots, consistently accounting for the redshift evolution of expected background sources beyond the clusters. For each projection along the simulation axes, we select particles in a slice of depth  $\pm 5$  Mpc ( $3.4 h^{-1}$  Mpc) in front and behind the cluster and  $\pm 2.5$  Mpc ( $1.7 h^{-1}$  Mpc) from the projected cluster centre in the considered plane of the sky. The depth of the projection along the line of sight has been chosen as a compromise to include the neighbouring correlated structure and avoid including low-resolution particles in the lensing simulated maps. Our method used to smooth the mass distribution considers a smoothing length equal to the distance of the  $n^{\text{th}}$  neighbour particle, with  $n = 80$ . This is done for each particle species weighted according to their masses – dark matter, gas, star, and black hole – using Py-SPHViewer (for more details, we refer to *Benitez-Llambay 2015*) on a grid with a pixel resolution of  $2048 \times 2048$  and 5 Mpc on a side.

The convergence,  $\kappa$ , is obtained from the mass map by dividing the mass per pixel by its associated area to obtain the surface density,  $\Sigma(\theta)$ , and by the critical surface density,  $\Sigma_{\text{crit}}$  (*Bartelmann & Schneider 2001*) that can be read as:

$$\Sigma_{\text{crit}} \equiv \frac{c^2}{4\pi G} \frac{D_s}{D_l D_{ls}}, \quad (3)$$

where  $D_l$ ,  $D_s$ , and  $D_{ls}$  are the observer-lens, observer-source and source-lens angular diameter distances, respectively;  $c$  represents the speed of light and  $G$  the universal gravitational con-

stant. Our reference weak-lensing maps have been created assuming a fixed source redshift  $z_s = 3$ .

As an example, in Fig. 1, we show the convergence map obtained by collapsing the particles along the  $z$ -direction of the re-simulated box, considering one cluster at redshift  $z_l = 0.22$ : from left to right, we show the convergence obtained from the GadgetX, GIZMO-SIMBA, and DM-only run. Note that the colour code shown in this figure (blue, red, and green respectively for GadgetX, GIZMO-SIMBA, and DM-only) will be used throughout the paper. In all cases, the large-scale projected matter density distribution looks relatively similar, while the position of substructures differs due to the slightly different timings of evolution introduced by the presence of the collisional component.

From the convergence  $\kappa$ , we can write the lensing potential  $\psi$ , from the two-dimensional Poisson equation, as:

$$\Delta_{\theta} \psi(\theta) = 2 \kappa(\theta), \quad (4)$$

that we numerically solve in Fourier space using the Fast Fourier Transform (FFT) method. From Eq. 4, we can detail the two components ( $\gamma_1, \gamma_2$ ) of the pseudo-vector shear, as:

$$\gamma_1(\theta) = \frac{1}{2} \left( \frac{\partial^2 \psi(\theta)}{\partial x^2} - \frac{\partial^2 \psi(\theta)}{\partial y^2} \right), \quad (5)$$

$$\gamma_2(\theta) = \frac{\partial^2 \psi(\theta)}{\partial x \partial y}, \quad (6)$$

where  $x$  and  $y$  represent the two components of the vector  $\theta$ .

We use these equations to build shear maps that are then analysed in the next sections. For each cluster, we use the shear maps to simulate an observed surface mass density profile,  $\Delta\Sigma$ , by randomly sampling the field of view with a given number density of expected background sources. Notice that the real observable is the reduced shear,  $g = \gamma/(1 - \kappa)$ , which, in the weak lensing regime, we can approximate as  $g \simeq \gamma$ . We assume a background density of sources for weak lensing normalised to the total value of 30 galaxies per square arcmin, with a peak around  $z = 1$  (*Boldrin et al. 2012, 2016; Euclid Collaboration: Giocoli et al. 2024*). The excess surface mass density,  $\Delta\Sigma$ , shown in Fig. 2 is defined as  $\Delta\Sigma(\theta) = \bar{\Sigma}(< \theta) - \Sigma(\theta) \equiv \Sigma_{\text{crit}} \gamma_i(\theta)$ , with

$$\gamma_i(\theta_i) = -\gamma_1(x_i, y_i) \cos(2\phi_i) - \gamma_2(x_i, y_i) \sin(2\phi_i), \quad (7)$$

where  $(0,0)$  is the centre of the cluster by construction,  $\theta_i = (x_i^2 + y_i^2)^{1/2}$  and  $\phi_i = \arctan(y_i/x_i)$ .

The associated error bars account for the intrinsic shape of the background galaxies and the uncertainty on the mean value within the annulus (see [Euclid Collaboration: Giocoli et al. \(2024\)](#)), which can be read as:

$$\sigma_{\Delta\Sigma} = \sqrt{\sigma_{\langle\Delta\Sigma\rangle}^2 + \Sigma_{\text{crit}}^2 \frac{\sigma_e^2}{n_g \pi (\theta_2^2 - \theta_1^2)}}, \quad (8)$$

where  $\sigma_e = 0.3$  ([Hoekstra et al. 2004, 2011](#); [Kilbinger 2015](#); [Euclid Collaboration: Blanchard et al. 2020](#)) is the dispersion of the shape of background source galaxies, and  $\theta_1$  and  $\theta_2$  are the lower and upper bounds of the considered radial annulus. From [Fig. 2](#), we can notice that for this specific cluster, the run performed with the `GadgetX` code has a higher excess surface mass density than the other runs (`GIZMO-SIMBA` and `DM-only`) as evident from the bottom sub-panel of the figure.

### 2.3. Profile Model

In order to model the simulated weak-lensing profile, we adopt a smoothly truncated NFW density profile ([BMO, Baltz et al. 2009](#)), defined as:

$$\rho(r_{3D}|M_{200}, c_{200}, R_t) = \rho_{\text{NFW}}(r_{3D}|M_{200}, c_{200}) \left( \frac{R_t^2}{r_{3D}^2 + R_t^2} \right)^2, \quad (9)$$

with  $R_t = t R_{200}$  with  $t$  defined as the truncation factor. Following the results by [Oguri & Hamana \(2011\)](#), [Bellagamba et al. \(2019\)](#), and [Giocoli et al. \(2021\)](#) we will adopt a truncation radius  $R_t = 3 R_{200}$ . The total mass enclosed within  $R_{200}$ , i.e.,  $M_{200}$ , can be thought of as the normalisation of the model and as a mass proxy of the true enclosed mass of the dark-matter halo hosting the cluster ([Giocoli et al. 2012a](#)). Writing  $r_{3D}^2$  as the sum in quadrature between the sky projected coordinate  $r = D_d \theta$  and the line-of-sight  $\zeta$  coordinate, and integrating along  $\zeta$  we can write

$$\Sigma(r|M_{200}, c_{200}, R_t) = \int_0^\infty \rho(r, \zeta|M_{200}, c_{200}, R_t) d\zeta. \quad (10)$$

The differential excess surface mass density can then be written as:

$$\Delta\Sigma(r) = \frac{2}{r^2} \int_0^r r' \Sigma(r') dr' - \Sigma(r). \quad (11)$$

In order to model the data, we performed a Bayesian analysis using Monte Carlo Markov Chain approach, assuming a Gaussian log-likelihood between the model and the data <sup>2</sup> ([Marulli et al. 2016](#)) that can be read as:

$$\mathcal{L} \propto \exp\left(-\frac{1}{2}\chi^2\right), \quad (12)$$

where

$$\chi^2 = \sum_i \left( \frac{\Delta\Sigma_i(r_i) - \Delta\Sigma_{\text{model}}(r_i)}{\sigma_{\Delta\Sigma_i}} \right)^2, \quad (13)$$

and the sum extends to the number of radial bins. We set uniform priors for  $\log(M_{200}/[h^{-1} M_\odot]) \in [12.5, 16]$  and  $c_{200} \in [1, 15]$ , and let each MCMC chain run for 16 000 steps.

<sup>2</sup> <https://federicomarulli.github.io/CosmoBolognaLib/Doc/html>

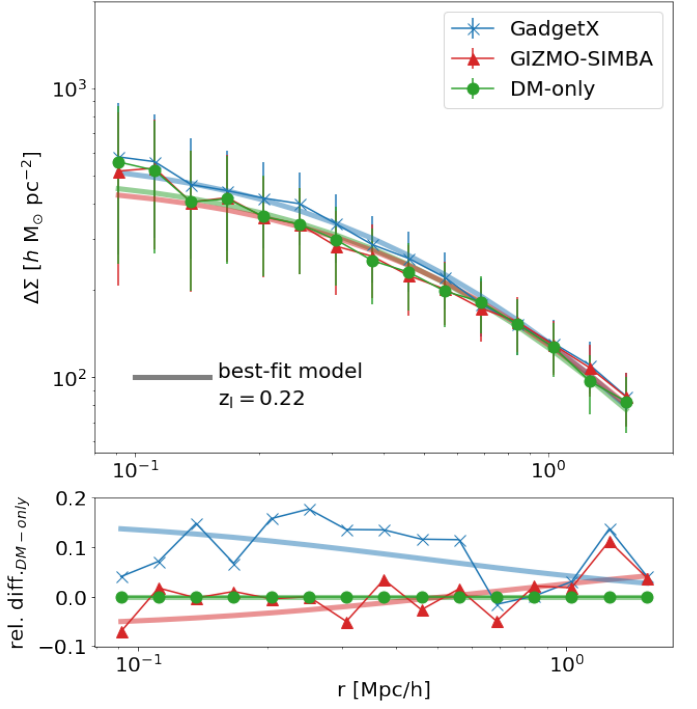


**Fig. 2.** Excess surface mass density profile of the projections displayed in [Fig. 1](#). The colours used for the data points, blue, red and green, correspond to the `GadgetX`, `GIZMO-SIMBA` and `DM-only` run, respectively. The bottom panel displays the relative difference with respect to the `DM-only` case. The best-fit models are shown using solid curves, coloured according to each considered case.

In [Fig. 2](#), the solid curves show the best-fit result as the model computed from the median values of the posterior distributions for the same considered cluster as in the previous figure. The bottom sub-panel displays the relative difference between the excess surface mass density measured — and modelled — in the hydro runs versus the `DM-only` case. From the figure, we can notice that the `GadgetX` simulated clusters presents a steepening toward the centre, 10% larger than the other two cases. In contrast, the hydro run `GIZMO-SIMBA` profile is quite close to the `DM-only` one.

In [Fig 3](#), we show the posterior distributions of the derived mass and concentration. We compare our results with respect to the parameters of the `DM-only` cluster. In particular, while all derived masses are consistent within  $1\sigma$  uncertainties with respect to the run with only dark matter, the concentration of the `GadgetX` run turns out to be more than  $1\sigma$  away from the `DM-only` case, as a consequence of the steeper projected profile toward the centre as displayed in [Fig. 2](#).

In [Fig. 4](#), we now consider all  $z = 0.22$  maps and show the average weak-lensing mass bias for all cluster projections with respect to either their corresponding true mass (on the left) or the true mass as measured in the `DM-only` simulation (on the right), this latter typically used in the halo mass function calibration ([Sheth & Tormen 1999](#); [Tinker et al. 2008](#); [Despali et al. 2016](#)). The right sub-panels show the PDF of the data of the three sets of simulations, while the top ones show the average relative uncertainties as a function of the corresponding rescaled mass. From the left panel, we conclude that despite the differences among the three simulation sets, they all provide the same answer for the weak-lensing bias and its scatter, implying that the differences in the baryonic physics counterbalance during the weak lensing derivation of the cluster mass. When we com-

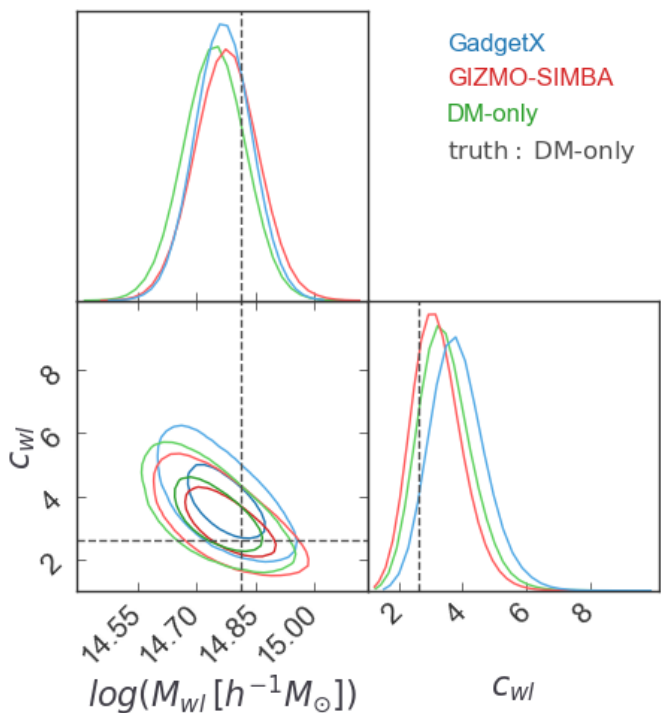


**Fig. 3.** Posterior distributions of derived weak-lensing mass and concentration from the three weak-lensing simulations of the cluster of Fig. 1 and Fig. 2. The dashed lines indicate the three-dimensional mass and concentration for the DM-only cluster run.

pare the hydro weak-lensing masses with the DM-only masses (right panel), we find that, on average, the two hydro-runs show a specular trend, reflecting the results from the single cluster shown in the previous figures. While the GadgetX weak-lensing masses reduce the DM-only bias, the GIZMO-SIMBA ones tend to be larger for smaller systems. Both codes have differences that tend to vanish when  $M_{200, \text{DM}} \gtrsim 10^{15} h^{-1} M_{\odot}$ , as displayed in the bottom sub-panel. This result and its dependence on the mass is linked to the fact that even starting from the same initial condition, GIZMO-SIMBA produces groups which are less massive than Gadget-X since its strong feedback pushes out a large fraction of the gas mass and thus slow down the overall matter accretion.

Euclid Collaboration: Giocoli et al. (2024) have presented the average cluster weak-lensing mass biases as a function of redshift, using the results of the GadgetX simulations. To complement their findings, in Fig. 5, we show the average weak-lensing mass biases with respect to the dark matter-only simulation mass as a function of redshift for the three simulation runs. In order to underline the dependence on the halo mass at each redshift, we split the cluster sample into two subsamples, containing clusters with  $M_{200, \text{DM}}$  larger or smaller than  $5 \times 10^{14} h^{-1} M_{\odot}$ . We colour-code the results by the DM-only mass. In general, we note that more massive clusters suffer from a smaller WL mass bias, as underlined by Euclid Collaboration: Giocoli et al. (2024), depending on the weak lensing signal-to-noise, modulated by the considered source redshift distribution. It is also worth mentioning that the GadgetX and GIZMO-SIMBA clusters have an opposite trend with respect to the DM-only simulation: while the former ones are on average higher by 1.2% (1.6%), the latter ones lower by 1.2% (3.7%), for the more massive (less massive) clusters with  $M_{200, \text{DM}} \geq 5 \times 10^{14} h^{-1} M_{\odot}$  ( $M_{200, \text{DM}} < 5 \times 10^{14} h^{-1} M_{\odot}$ ), respectively. The dotted lines display the redshift evolution of the mass biases with respect to the

considered three-dimensional hydrodynamical, again underlining that, in this case, the differences with respect to the corresponding true mass are only within a few per cent.

Before concluding this section, it is worth noticing that Lee et al. (2018) have underlined that the biases at small masses could be driven by the concentration priors and the positive correlation between concentration and mass; moreover, while Euclid Collaboration: Ragagnin et al. (2024) highlighted that this could be due to the poor NFW-fit for those systems, Giocoli et al. (2014); Euclid Collaboration: Giocoli et al. (2024) emphasised that the weak lensing signal-to-noise ratio and halo triaxiality could play the important role.

### 3. Weak-Lensing Mass-Richness Relations

This section presents the weak-lensing mass-richness relation in our simulated mass-selected cluster sample.

We compute the cluster richness using the position of haloes and subhaloes in the simulated field of view of 5 Mpc on the side. Specifically, from each halo projection we count the total number of subhaloes and haloes in a cylinder with a radius equal to  $R_{200}$ , with respect to the cluster centre, and height equal to  $\Delta H = 10$  Mpc that corresponds to roughly  $\Delta z = 0.002 \times (1 + z)$ , which represents an optimistic case reachable with spectroscopic data (Laureijs et al. 2011; Jauzac et al. 2021; Caminha et al. 2023; D’Addona et al. 2024; Mainieri et al. 2024). The richness of the simulated clusters is computed by considering a minimum stellar mass cut mimicking the observational measure that depends on the survey depth and the corresponding magnitude limit of the data set, photometric properties, and stellar mass determination.

In Fig. 6, we show the convergence map, haloes and subhaloes in the  $(x, y)$  plane of our test halo at redshift  $z = 0.22$  from Fig. 1. Black circles show the location of cluster subhaloes, the red-filled triangles all haloes in the cylinder projected within  $R_{200}$  including also the main halo. In this case, we consider all (sub)haloes with  $M_{\text{star}} > 0$ . The pink crosses mark the haloes in a cylindrical ring between 2 and 3.5 times  $R_{200}$ . These are chosen far enough from the cluster to be representative of the halo projected density in the field. This sample will be used to estimate the number of contaminant haloes, i.e. subtracting the local background, to correct the cluster richness (Andreon & Bergé 2012), which we define as:

$$\lambda_{\text{obs}}(M_{\text{star}} > M_{\text{star, min}}) = n_{\text{Subhaloes}} + n_{\text{Haloes}} - \frac{4}{33} n_{\text{Outer Haloes}} \quad (14)$$

The geometrical factor  $4/33$  has been computed by rescaling the density of haloes in the cylindrical ring between 2 and 3.5  $R_{200}$  to account for the difference in area. This richness estimate is computed individually for each cluster projection, while for each cluster, the intrinsic richness is calculated from  $\lambda_{\text{int}} = n_{\text{Subhaloes}} + 1$ , i.e. number of satellite galaxies in subhaloes within  $R_{200}$ , plus the central.

As reference cases, in Fig. 7, we display the weak-lensing mass versus the richness for clusters at  $z = 0.22$  simulated using the GadgetX prescription. In the four panels we consider different stellar mass cuts, from  $M_{\text{star, min}} = 10^{10} h^{-1} M_{\odot}$  to  $M_{\text{star, min}} = 10^{10.75} h^{-1} M_{\odot}$  with a step  $d \log(M_{\text{star, min}}) = 0.25$ . For each  $M_{\text{star, min}}$  case, we display three different sets of data points. The first one is the true mass-intrinsic richness relation that considers the true  $M_{200}$  and all sub-halos within  $R_{200}$  (magenta triangles, as in Chen et al. 2024); in this case, there are no projection effects when counting the member galaxies, while bias and

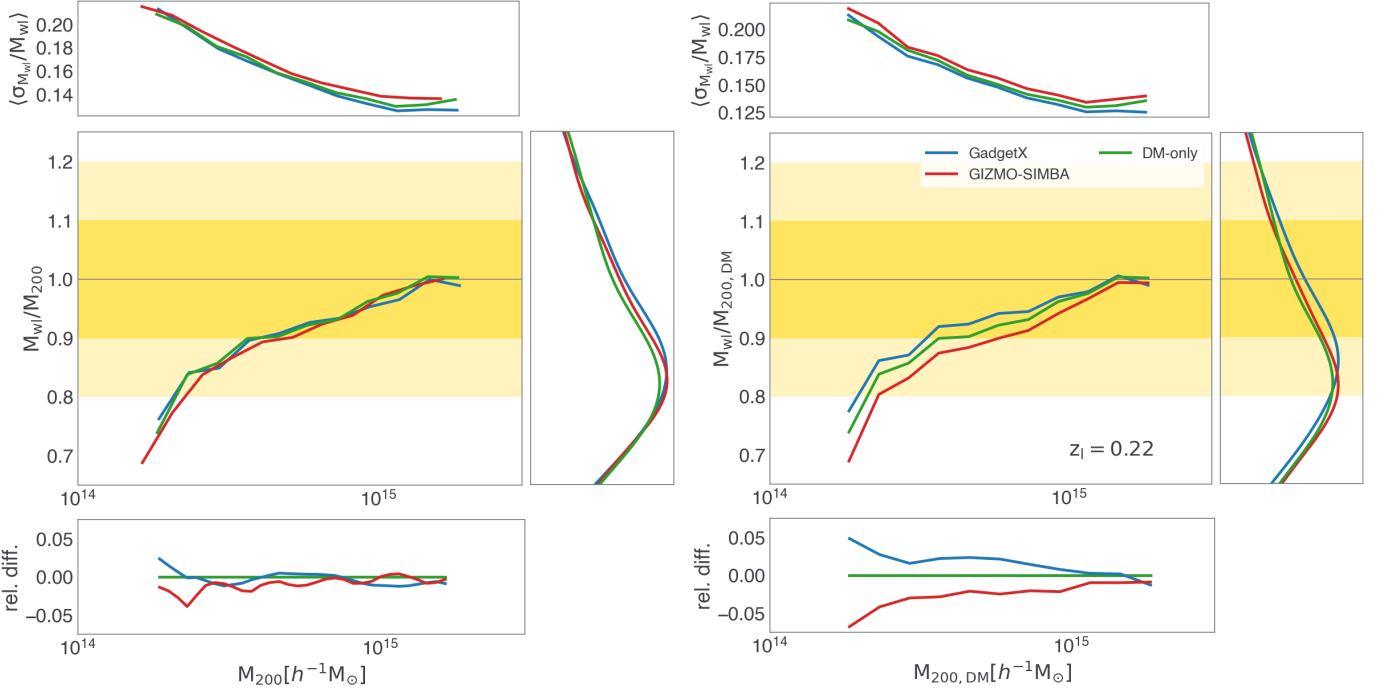


**Fig. 4.** Average weak-lensing mass biases as a function of the corresponding three-dimensional masses. On the left, the weak lensing masses are relative to their respective total mass; on the right, they are always related to the total mass of the DM-only runs. The top and bottom sub-panels show the mean relative uncertainties and the relative differences as a function of considered three-dimensional reference mass, respectively. The right panels display the distribution of the weak-lensing mass biases over all cluster masses.

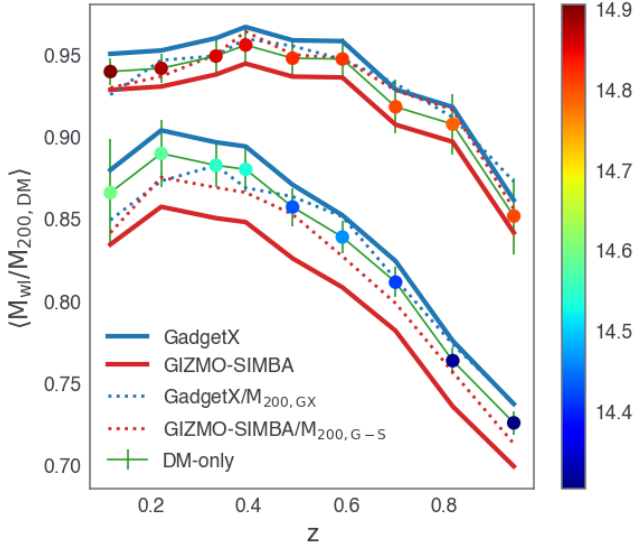


**Fig. 5.** Average weak-lensing mass biases as a function of redshift. Data points with error bars, colour-coded according to their DM-only corresponding mass, show the dark matter-only run results. Blue and red lines refer to the GadgetX and GIZMO-SIMBA hydro simulation cases, respectively. Dotted and solid lines show the bias in relation to the hydro mass and the DM-only mass, respectively.

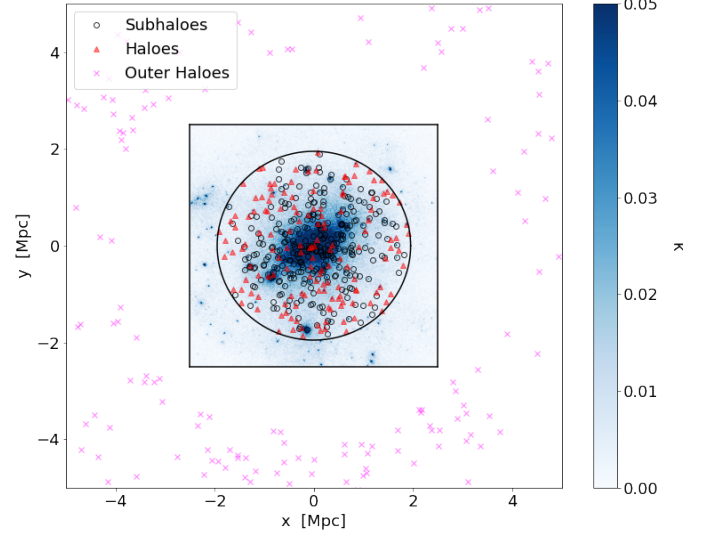


**Fig. 6.** Halo and Subhalo distribution in the projection  $x$ - $y$  considering a field of view of 10 Mpc on a side and  $\pm 5$  Mpc along the line of sight,  $\Delta H = 10$  Mpc, for the GadgetX cluster run. Black circles show the location of the centre of all subhaloes within the halo radius  $R_{200}$ , red triangles are all haloes which, in projection, fall within the halo radius, and magenta crosses are all haloes that, in projection, lie in a ring between 2 and  $3.5 R_{200}$  which we term outer haloes. The blue map is the corresponding region where we simulate the weak-lensing cluster signal.

uncertainties on the cluster mass are set to zero. Second, combining all the three cluster projections, the green circles show the case where we consider all satellite galaxies in a cylinder of radius  $R_{200}$ , plus the central, and adopt as cluster mass  $M_{wl}$ , the one computed modelling the weak-lensing simulated data. Third, the blue-filled circles, with the corresponding error bars, show the observed richness with the corresponding Poisson un-

certainty and the weak-lensing mass  $M_{wl}$ , calculated as described in Section 2.3. For comparison, in the top two panels, the magenta dashed lines show the results by Chen et al. (2024), who modelled the intrinsic cluster richness as a function of the true mass  $M_{200}$ , calibrated up to  $M_{\text{star, min}} \simeq 10^{10} h^{-1} M_{\odot}$ , using the same simulations of this work. Note that this model already fails

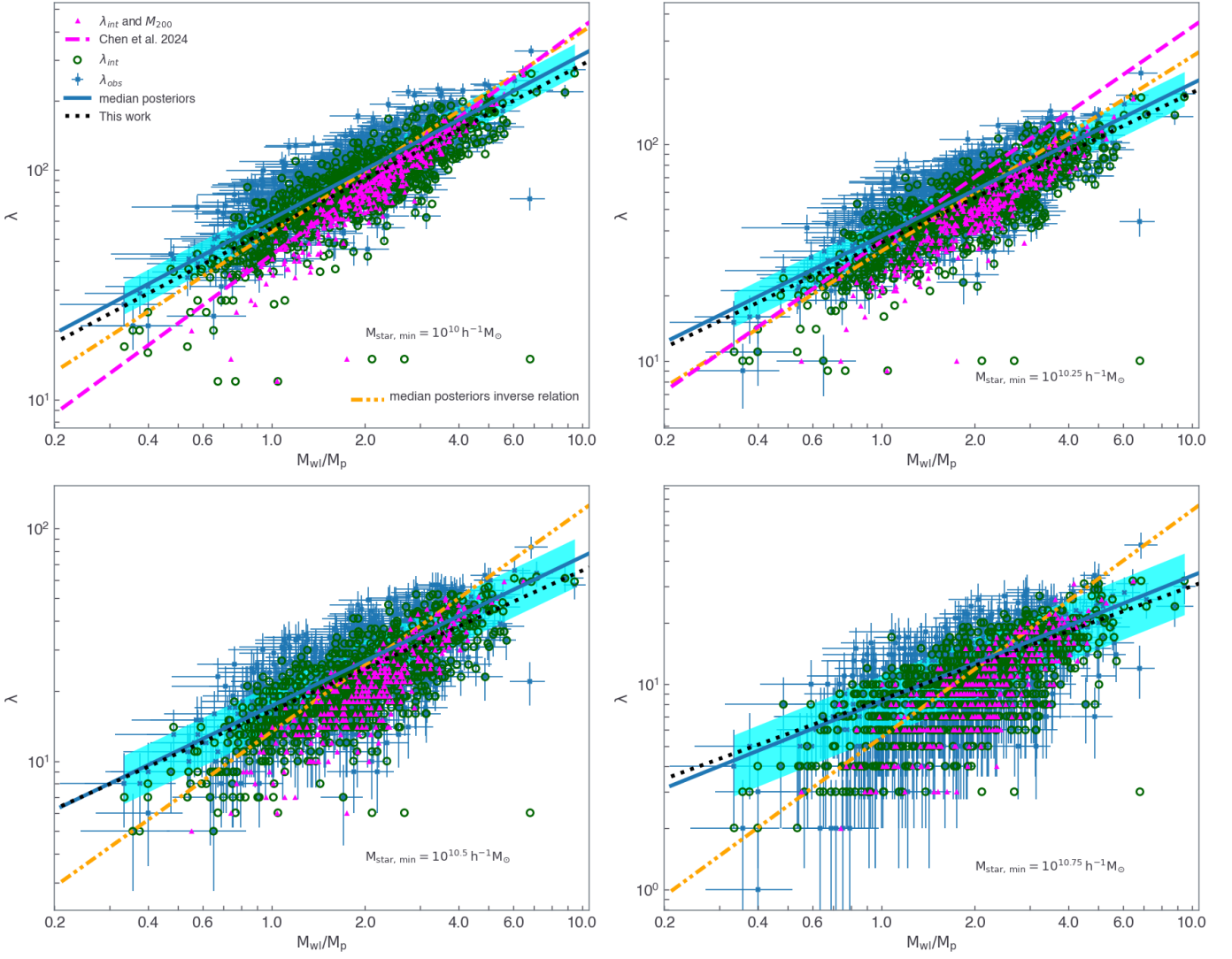


**Fig. 7.** Weak-lensing mass-observed richness relation measured for the clusters at redshift  $z = 0.22$  run with *GadgetX*. The different panels consider different minimum stellar mass cuts  $M_{\text{star, min}}$ , from  $10^{10}$  to  $10^{10.75} h^{-1} M_{\odot}$ . The weak-lensing masses  $M_{\text{wl}}$  are rescaled with respect to the pivot value  $M_{\text{p}} = 3 \times 10^{14} h^{-1} M_{\odot}$ . The blue points with the corresponding error bars show the results for the observed richness calculated as in Eq. 14 and the derived weak-lensing mass from the tangential shear profile. For the magenta triangles, the mass is not  $M_{\text{wl}}$ , but  $M_{200}$ ; correspondingly we show the number  $\lambda_{\text{int}}$  of galaxies within  $R_{200}$ . The green circles show the results when using  $M_{\text{wl}}$  and the number of subhaloes in the projected  $R_{200, 2D}$ . The blue solid line displays the results of our fit performed using MCMC on the blue data points, and in cyan, the  $1\sigma$  uncertainty. The orange dash-dotted line is the best fit of the inverse relation; see Eq. 18. Black dotted lines display the model presented in this work.

to describe the magenta triangle in the top-left panel for which  $M_{\text{star, min}} = 10^{12.5} h^{-1} M_{\odot}$ . In all panels of Figure 7, we show two log-log relations between mass and richness described here for different considered minimum stellar mass cuts with computing the richnesses. Notice that the scatter increases at higher stellar mass cuts and that the inverse relation (displayed with a dot-dashed orange line) differs from the weak-lensing mass-richness relation when the scatter and the errors in the richness are larger.

#### • Weak-Lensing Mass-Observed Richness relation (WLOR)

The solid blue lines display the best result of the linear regression model:

$$\langle \log(\lambda_{\text{obs}}(M_{\text{star}} > M_{\text{star, min}}) | M_{\text{wl}}) \rangle = A + B \log\left(\frac{M_{\text{wl}}}{M_{\text{p}}}\right), \quad (15)$$

where masses are rescaled with respect to the pivot value  $M_{\text{p}} = 3 \times 10^{14} h^{-1} M_{\odot}$ , the intercept  $A$  and the slope  $B$  are computed

using an MCMC Bayesian inference model assuming a Gaussian likelihood. The latter, accounting for error bars on both axes, is written as:

$$\mathcal{L} \propto \exp\left\{-\frac{1}{2} \sum_i \left[\frac{\log(\lambda_{\text{obs}, i}) - \log(\lambda_i)}{\sigma_i}\right]^2\right\}, \quad (16)$$

with

$$\sigma_i^2 = \sigma_{\log \lambda_{\text{obs}, i}}^2 + B^2 \sigma_{\log M_{\text{wl}, i}}^2, \quad (17)$$

where  $\sigma_{\log \lambda_{\text{obs}, i}}$  and  $\sigma_{\log M_{\text{wl}, i}}$  are the uncertainties relative to the  $i$ -cluster. We assume wide uniform priors for  $A$  and  $B$ :  $A \in [-50, 50]$  and  $B \in [-1, 5]$ . The cyan-shaded regions in Fig. 7 display the  $1\sigma$  uncertainty of the linear regression model parameters. From the figure, we notice that  $\lambda_{\text{int}}$  is a conservative lower limit of the measured cluster richness with respect to  $\lambda_{\text{obs}}$ . The observed richness is related to the weak-lensing mass by a power-law relation  $\lambda_{\text{obs}} \propto M_{\text{wl}}^B$ , and considering that both



observables have their corresponding associated uncertainties, it follows that  $M_{wl} \propto \lambda_{\text{obs}}^{1/B}$  (Andreon 2010; Andreon & Bergé 2012; Andreon 2012; Andreon & Hurn 2013; Andreon 2016).

### • Observed Richness-Weak-Lensing Mass relation (ORWL)

The orange dash-dotted lines in Fig. 7, display the *inverse* of the median posteriors of the linear regression:

$$\left\langle \log \left( \frac{M_{wl}}{M_p} \right) \right\rangle = C + D \log (\lambda_{\text{obs}}(M_{\text{star}} > M_{\text{star, min}}) | M_{wl}), \quad (18)$$

that relates the weak-lensing mass to the observed richness by the power-law relation  $M_{wl} \propto \lambda_{\text{obs}}^D$ , underlining that  $D \neq 1/B$ . For likelihood modelling of the linear regression parameters  $C$  and  $D$ , we use Equation 16 substituting the richness with the mass, and consistently, their associated uncertainty propagation, which can be read as:

$$\sigma_i^2 = \sigma_{\log M_{wl,i}}^2 + D^2 \sigma_{\log \lambda_{\text{obs},i}}^2. \quad (19)$$

While Figure 7 refers only to GadgetX, in the two panels of Fig. 8, we show the WLOR relation in both hydro-runs, considering the two largest stellar mass cuts: GadgetX in blue and GIZMO-SIMBA in red, respectively. The results of the linear regression Bayesian inferred model are shown with the corresponding coloured solid lines and the shaded  $1 \sigma$  uncertainty. The figure shows that the results from both hydro runs are consistent within the shaded uncertainty region derived from the independent propagated uncertainties in the MCMC analyses of the two hydro runs. The right sub-panels show the PDF of the scatter of the observed richness with respect to the corresponding linear regression model at a fixed weak-lensing mass, with the shaded region marking the corresponding scatter  $\sigma_{\log \lambda_{\text{obs}}}$ . It is worth underlining that, on average, the scatter in the GIZMO-SIMBA cluster simulations is marginally larger than the one measured in GadgetX. Generally, the parameters  $A$  and  $B$  of the linear regression model (see Eq. 15) and  $\sigma_{\log \lambda_{\text{obs}}}$  depend on the stellar mass cut  $M_{\text{star, min}}$ , redshift  $z$  and the hydro simulation considered.

### 3.1. Redshift Evolution

Our analysis aims to model the observed richness-weak-lensing mass relations for clusters at different redshifts from  $z = 0.12$  up to  $z = 0.94$ . In order to do so, we model all the nine considered simulation snapshots and analytically describe the redshift evolution of the parameters describing this scaling relation, namely the intercept, the slope and the scatter.

We summarise the results of the WLOR parameters in Fig. 9, where they are displayed as a function of the cluster redshifts, the four considered stellar mass cuts and both hydro runs – in blue and red for the GadgetX and GIZMO-SIMBA, respectively. We note that the intercept  $A$  is consistent with being redshift independent and increasing with the stellar mass cut. GadgetX clusters have slightly larger values than the GIZMO-SIMBA ones. The slope parameter  $B$  and the scatter  $\sigma_{\log \lambda_{\text{obs}}}$  instead manifest a moderate redshift dependence. A second-order polynomial  $a + bz + cz^2$ , fixing  $c = -0.42$  independently of the stellar mass cut, describes quite well the slope, while the scatter is well fit by a linear relation. In particular, the WLOR relations of the GadgetX clusters have a steeper slope  $B$  than the GIZMO-SIMBA ones. Notice that the slope parameter is relatively constant up to

$z \approx 0.55$ , after which we are sensitive to the variation and the cut-off of the stellar mass function (Chen et al. 2024) reflecting the complex interplay between galaxy formation, environmental effects, and hierarchical structure formation. The black lines and curves in the three panels, styled according to the different considered minimum stellar mass cuts  $M_{\text{star, min}}$ , represent the best-fit models combining both hydro-runs. In Table 1, we summarise the best-fit parameters of redshift evolution and for different stellar mass cuts. The dotted black lines – labelled as "This work" or as "This work  $M_{wl}$ " – reported in the Figs. 7, 8 and 11 have been computed adopting the best-fit model parameters as reported in Table 1. We follow the same procedure, combining the results of both hydro simulations to model the redshift evolution of the parameters of the ORWL relation  $C$ ,  $D$  and  $\sigma_{\log M_{wl}}$ , as reported in Table 2.

### 3.2. Comparison with the literature

In Fig. 10, we compare our ORWL relation with different results from the literature. We follow Table 5 by McClintock et al. (2019) to rescale the various redMaPPer (Rykoff et al. 2014; Rozo et al. 2015; Rykoff et al. 2016) considered richnesses. We show our model for  $M_{\text{star, min}} = 10^{10} h^{-1} M_{\odot}$  which is consistent with different results reported here. In particular, the work by McClintock et al. (2019) constrains the richness-mass scaling relation for galaxy clusters in the Dark Energy Survey Year 1 data using weak lensing. Clusters are divided into bins of richness ( $\lambda \geq 20$ ) and redshift ( $0.2 \leq z \leq 0.65$ ), with mean masses measured via stacked lensing signals. The analysis, incorporating detailed systematic error considerations, provides very precise measurements, highlighting the potential of DES for cluster cosmology. Baxter et al. (2018), using CMB maps from the South Pole Telescope survey and a cluster catalogue from the Dark Energy Survey Year 1 data (with mean redshift  $z = 0.45$ ), detects CMB lensing by clusters at a high significance. In that paper, the lensing signal constrains the mass-richness scaling relation with approximately 17% precision. It is worth underlining that this analysis is primarily limited by statistical noise, with notable systematic contributions from the thermal SZ effect and cluster miscentering. Both Simet et al. (2017) and Murata et al. (2018) constrain the relationship between optical richness and halo mass for SDSS redMaPPer clusters in the redshift range  $0.10 \leq z \leq 0.33$ . However, they adopt a different richness binning selection criteria and a diverse methodology to model the stacked weak-lensing cluster profiles: while Simet et al. (2017) assume an analytical model, Murata et al. (2018) use forward modelling with a calibrated emulator based on N-body simulations. Melchior et al. (2017) based their analysis of the richness-weak-lensing mass relation on shear measurements of over 8,000 redMaPPer galaxy clusters in the Dark Energy Survey Science Verification (SV) data. Their analysis incorporates models addressing different systematic uncertainties and fits a scaling relation for mass, richness, and redshift. In particular, their findings agree with prior weak-lensing calibrations and extend the calibrated redshift range for redMaPPer clusters  $0.3 \leq z \leq 0.8$ . Mantz et al. (2016) constrain the scaling relations between redMaPPer richness and individual weak-lensing mass measurements for an X-ray selected cluster sample of Weighing the Giants project (von der Linden et al. 2014). Saro et al. (2015) cross-match galaxy clusters detected via the Sunyaev-Zel'dovich effect (SZE) in the South Pole Telescope SPT-SZ survey with optically identified clusters from the Dark Energy Survey (DES-SV). For a total of 25 clusters, they confirm consistency between SPT-SZ and redMaPPer cluster samples but find mild tension

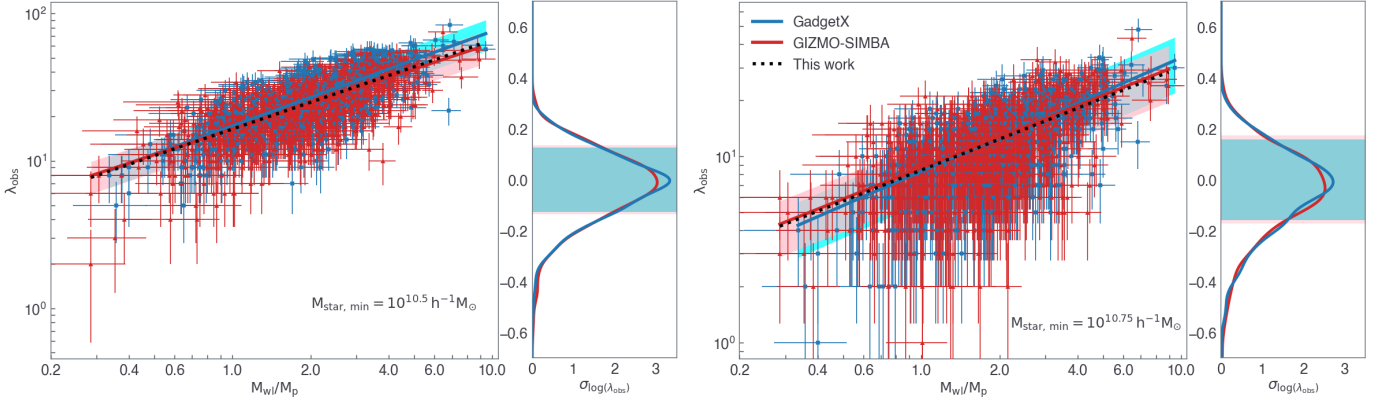


**Fig. 8.** Weak-lensing mass-observed richness relation measured for the clusters at redshift  $z = 0.22$  run with both hydrocodes GadgetX in blue and GIZMO-SIMBA in red, respectively. The blue points are thus the same from Figure 7. The solid lines show the linear regression model results, with the shaded region indicating the  $1\sigma$  uncertainty on the intercept and slope parameters. The right sub-panel shows the probability distribution function of observed richness at a given  $M_{WL}$ , to the best-fit linear model, with the shaded region marking the corresponding scatter  $\sigma_{\log \lambda_{\text{obs}}}$ .

**Table 1.** Weak-lensing mass richness relation parameters as a function of redshift  $z$  and considering different stellar mass cut  $M_{\text{star,min}}$ , as shown in the left column.

$M_{\text{star,min}}$	Intercept: $A$	Slope: $B$	$\sigma_{\log \lambda_{\text{obs}}}$
$10^{10} M_{\odot}/h$	$1.74 \pm 0.03$	$0.664 \pm 0.006 + 0.313 \pm 0.010 z - 0.42 z^2$	$0.100 \pm 0.002 + 0.017 \pm 0.004 z$
$10^{10.25} M_{\odot}/h$	$1.54 \pm 0.04$	$0.645 \pm 0.006 + 0.310 \pm 0.011 z - 0.42 z^2$	$0.109 \pm 0.003 + 0.019 \pm 0.004 z$
$10^{10.5} M_{\odot}/h$	$1.22 \pm 0.02$	$0.544 \pm 0.008 + 0.361 \pm 0.014 z - 0.42 z^2$	$0.126 \pm 0.003 + 0.045 \pm 0.005 z$
$10^{10.75} M_{\odot}/h$	$0.93 \pm 0.03$	$0.504 \pm 0.010 + 0.313 \pm 0.018 z - 0.42 z^2$	$0.152 \pm 0.004 + 0.065 \pm 0.007 z$

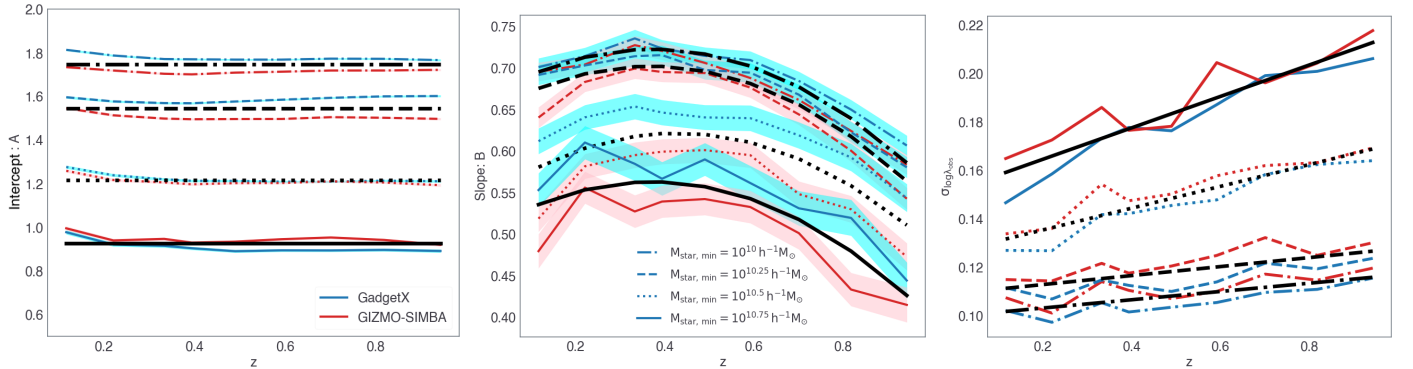


**Fig. 9.** Intercept  $A$ , slope  $B$  and scatter  $\sigma_{\log \lambda_{\text{obs}}}$  at a fixed weak-lensing cluster mass as a function of redshift. Blue and red curves refer to the two hydro simulations: GadgetX and GIZMO-SIMBA, respectively. In all panels, the results referring to a given stellar mass cut are reported with different line styles. The black curves show the best-fit models as a function of redshift, combining both hydro run results at a fixed stellar mass cut. The best-fit values are reported in Table 1.

in some matching expectations. Positional offsets between optical and SZE clusters follow a bimodal distribution. Bellagamba et al. (2019) and Lesci et al. (2022a) use a different optical cluster finder: AMICO (Radovich et al. 2017; Bellagamba et al. 2018; Maturi et al. 2019). AMICO leverages galaxy luminosity, spatial distribution, and photo- $z$  data without relying on colour-based selection, minimizing biases from red-sequence detection and also providing a galaxy catalogue with probabilistic cluster associations. In particular, purity, completeness, and property uncertainties are evaluated with mock catalogues derived directly from the data, avoiding relying on numerical or semi-analytic models, such as the one implemented in SinFoniA (Maturi et al. 2019), as performed in KiDS-DR3 (de Jong et al. 2017). It is important to underline that while Bellagamba et al. (2019) model the AMICO richness weak-lensing mass relation using only a stacked sample of clusters in redshift and richness, Lesci et al. (2022a) include

in the analyses a model for the redshift evolution of the cluster mass function. Apart from the different survey coverages, photo- $z$  and depth between DES and KiDS-DR3 in inducing different richness-mass relations, redMaPPer and AMICO have separate methodologies. The redMaPPer algorithm relies on identifying the red sequence of galaxies and assumes clusters have a dominant population of red, passively evolving galaxies; on the other hand, AMICO does not rely on galaxy colours or the red sequence and uses a combination of galaxy luminosity, spatial distribution, and photometric redshifts, making it less dependent on the presence of red galaxies. As for cluster richness, redMaPPer directly measures richness based on red-sequence galaxies, while AMICO calculates richness probabilistically, incorporating all galaxies in a cluster and their likelihood of belonging based on a spatial threshold in magnitude depending on the survey magnitude limit and redshift information. The complexity

**Table 2.** Observed richness weak-lensing mass relation parameters as a function of redshift  $z$  and considering different stellar mass cut  $M_{\text{star,min}}$ , as shown in the left column. The last column presents the redshift evolution of the logarithm of the weak-lensing mass at a given observed richness.

$M_{\text{star,min}}$	Intercept: $C$	Slope: $D$	$\sigma_{\log M_{\text{wl}}}$
$10^{10} M_{\odot}/h$	$-1.90 \pm 0.05$	$1.12 \pm 0.02 + 0.10 \pm 0.08 z - 0.18 \pm 0.08 z^2$	$0.126^{0.003} + 0.027^{0.006} z$
$10^{10.25} M_{\odot}/h$	$-1.62 \pm 0.05$	$1.09 \pm 0.02 + 0.08 \pm 0.08 z - 0.18 \pm 0.08 z^2$	$0.133^{0.004} + 0.032^{0.007} z$
$10^{10.5} M_{\odot}/h$	$-1.15 \pm 0.04$	$1.04 \pm 0.02 + 0.17 \pm 0.09 z - 0.40 \pm 0.09 z^2$	$0.155^{0.005} + 0.050^{0.009} z$
$10^{10.75} M_{\odot}/h$	$-0.73 \pm 0.04$	$0.88 \pm 0.02 + 0.37 \pm 0.09 z - 0.60 \pm 0.08 z^2$	$0.171^{0.006} + 0.073^{0.010} z$

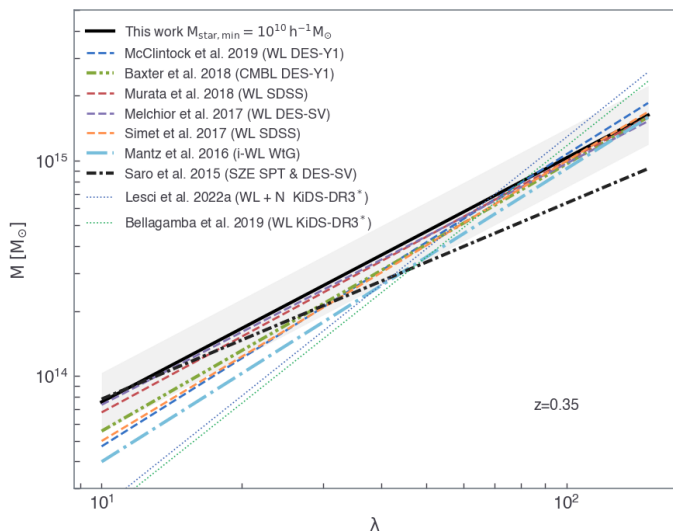


**Fig. 10.** Observed richness-weak-lensing mass relation comparison with different literature results. We compute our model considering an observed richness with a minimum stellar mass of  $M_{\text{star,min}} = 10^{10} h^{-1} M_{\odot}$  and the parameters have been calculated at  $z = 0.35$ . All redMaPPer (Rykoff et al. 2014) richness definitions have been rescaled to DES-Y1 by (McClintock et al. 2019) (see their Tab. 5). The two dotted lines referring to KiDS-DR3 clusters from (Lesci et al. 2022a) and (Bellagamba et al. 2019) have been computed with the AMICO cluster finder algorithm (Maturi et al. 2019).

and the dissimilarity of the two methods may explain the differences in the observed cluster population in Fig. 10. From a numerical simulation perspective, selecting galaxies based solely on a specific stellar mass threshold aligns more closely with the redMaPPer richness definition. This is illustrated by the solid black line in the figure, while the shaded region represents the  $\sigma_{\log M}$  as modelled in the Three Hundred clusters, reported in the fourth column in Table 2. With a few exceptions, the simulated ORWL relation agrees with the observational data, in particular, once the richness is above or equal to 30.

#### 4. True Mass-Richness Relations

The observed richness could also be directly used as a true mass proxy. In order to calibrate the relation with the true mass of the cluster, it is worth underlining that for each cluster we have three observed richness estimates, depending on the projection we are looking at, and one true mass  $M_{200}$  defined as the spherical mass within the radius  $R_{200}$  which encloses 200 times the critical co-moving density of the universe  $\rho_c(z)$  at the considered redshift. We model the linear regression between  $M_{200}$  and  $\lambda_{\text{obs}}$ , and at different redshifts, using the same methodology of the previous section. In our MCMC analysis, we adopt the same likelihood

as in Eqs. 16 and 17, neglecting the uncertainty on the mass and considering only the Poissonian error on the observed richness.

In Fig. 11, we display the true mass-observed richness relation for clusters at  $z = 0.22$  for both hydro-runs and the two highest stellar mass cuts. In both panels, the blue and red solid lines display the best-fit linear regression models computed from the median parameters of the posterior distributions. Since, in this case, we have the uncertainty only on the y-axis, we can directly invert  $\lambda_{\text{obs}} \propto M_{200}^B$  into  $M_{200} \propto \lambda_{\text{obs}}^{1/B}$ . The black dotted lines in the figure represent the linear regression models adopting the best-fit parameters as in Table 1, as computed for the observed richness-weak-lensing mass relation. The dot-dashed magenta lines represent the linear regression model for the observed richness-true mass case, the parameters of which are summarised in Table 3, obtained by combining the results of both hydro-runs. From the figure, we can notice that, on average, the difference between the black dotted and magenta dot-dashed lines reflects the weak-lensing mass bias as described in details by Euclid Collaboration: Giocoli et al. (2024): the weak-lensing mass of low mass clusters is, on average, more biased low than that of high mass systems with respect to the true cluster mass. Notice that the difference between the black-dotted and the dot-dashed magenta is also guided by the dispersion of the observed richnesses.

As previously discussed, we model the evolution of the intercept  $A$ , the slope  $B$  and the scatter  $\sigma_{\log \lambda_{\text{obs}}}$  as a function of redshift and for the four considered stellar mass cuts, in the true mass-observed richness relation. We also note that, in this case, the intercept is redshift-independent, the slope has a second-order polynomial dependence on  $z$  but with the second-order term coefficient  $c = -0.18$  and the scatter of the observed richness at a given true mass  $M_{200}$  depends linearly with redshift. It is worth underlining that the scatter of the observed richness at a fixed true mass is smaller than that at a fixed weak-lensing mass at a given redshift and stellar mass cut.

#### 5. Summary and Conclusions

Cosmological numerical simulations play an important role in guiding cluster cosmology studies. Weak gravitational lensing is the leading method in reconstructing galaxy clusters' projected matter density distribution. However, derived weak-lensing masses are biased low with respect to the true tridimensional mass, which is used in the halo mass function models.

Using state-of-the-art hydrodynamical simulations, in this work, we quantify the average weak-lensing bias dependences of two hydro-solvers GadgetX and GIZMO-SIMBA and compare with respect to a DM-only one (Tinker et al. 2008; Sheth & Tormen 1999; Despali et al. 2016). Using cluster random projections, we also calibrate the weak-lensing mass-richness relation and its inverse and compare our findings with different literature results. In what follows, we summarise our main results:

- all weak-lensing masses are, on average, negatively biased with respect to the corresponding true mass (Meneghetti

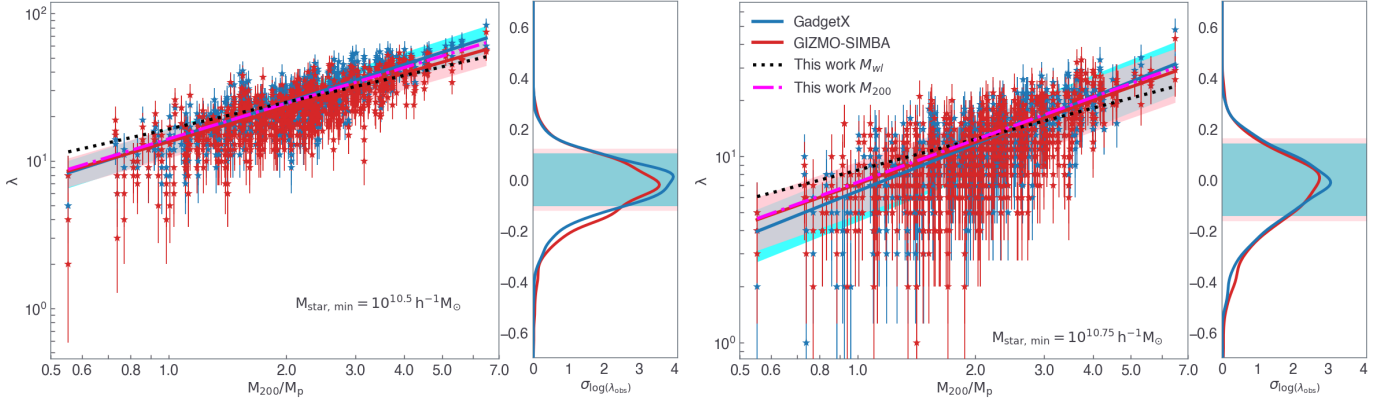


**Fig. 11.** True mass-observed richness relation for the clusters at redshift  $z = 0.22$  as measured in both hydro-runs. The solid lines show the linear regression model results, with the shaded region indicating the  $1\sigma$  uncertainty on the intercept and slope parameters. The right sub-panel shows the probability distribution function of the  $\lambda_{\text{obs}}$  with respect to the corresponding best-fit linear model, with the shaded regions marking the corresponding scatter  $\sigma_{\log \lambda_{\text{obs}}}$ . The dotted black lines exhibit the model for the richness weak-lensing mass relation, as described in the last section.

**Table 3.** True mass  $M_{200}$ -richness relation parameters as a function of redshift  $z$  and considering different stellar mass cut  $M_{\text{star},\text{min}}$ , as shown in the left column.

$M_{\text{star},\text{min}}$	Intercept: $A$	Slope: $B$	$\sigma_{\log \lambda_{\text{obs}}}$
$10^{10} M_{\odot}/h$	$1.68 \pm 0.03$	$0.847 \pm 0.005 + 0.206 \pm 0.008 z - 0.18 z^2$	$0.062 \pm 0.002 + 0.032 \pm 0.004 z$
$10^{10.25} M_{\odot}/h$	$1.48 \pm 0.05$	$0.855 \pm 0.006 + 0.161 \pm 0.011 z - 0.18 z^2$	$0.077 \pm 0.003 + 0.031 \pm 0.003 z$
$10^{10.5} M_{\odot}/h$	$1.15 \pm 0.01$	$0.780 \pm 0.009 + 0.145 \pm 0.016 z - 0.18 z^2$	$0.104 \pm 0.004 + 0.056 \pm 0.006 z$
$10^{10.75} M_{\odot}/h$	$0.86 \pm 0.03$	$0.757 \pm 0.012 + 0.049 \pm 0.022 z - 0.18 z^2$	$0.136 \pm 0.005 + 0.074 \pm 0.008 z$

et al. 2007b, 2010a,b; Lee et al. 2018). While the ratio between the weak-lensing masses of GadgetX clusters and the three-dimensional DM-only ones are a few per cent higher, the ones derived from GIZMO-SIMBA are lower probably due to the shallower inner slope of the total density profile due to the strong AGN feedback (Meneghetti et al. 2023); when WL masses are rescaled with respect to the corresponding three-dimensional ones all runs provide the same answer for the weak lensing mass bias and its scatter, and their redshift evolution;

- using halo and subhalo projected positions, we derive the observed richness accounting for local background contaminants;
- the weak-lensing mass-observed richness relations derived from both hydrodynamical simulations are consistent within  $1\sigma$  because of the propagated uncertainties; accordingly, we average the linear regression parameters from these simulations in our final model.
- while the intercept parameter is redshift-independent and varies with the minimum stellar mass cut used to define the cluster richness, the slope, almost constant up to redshift  $z = 0.55$ , changes with redshift following a second-order polynomial;
- the redshift evolution of the scatter of the observed richness (weak-lensing mass) at a fixed weak-lensing mass (observed richness) linearly increases with redshift, and the stellar mass cut  $M_{\text{star},\text{min}}$ ;
- our model for observed richness-weak-lensing mass is in good agreement with different literature results based on SDSS redMaPPer clusters when considering a minimum stellar mass cut  $M_{\text{star},\text{min}} = 10^{10} h^{-1} M_{\odot}$ ;
- in our last section, we derive the linear regression parameters and their dependence on  $z$  and  $M_{\text{star},\text{min}}$  for the true mass-observed richness relation; we find that the scatter of  $\lambda_{\text{obs}}$  at

a given true mass is smaller than the scatter at a given weak-lensing mass.

Numerical simulations have been extensively used to model the cluster mass function as a function of redshift and overdensity, along with their dependence on cosmology. However, the three-dimensional overdensity mass of clusters is not directly observable, and its reconstruction requires high-quality data and calibration with advanced numerical simulations. By combining this with other mass proxies obtained from multi-band observations, well-calibrated mass-observable relations can be developed to estimate galaxy cluster masses for larger samples with known observable properties. To conclude, it is important to underline that establishing and quantifying the relationship between weak-lensing cluster mass, richness, and potential systematics from baryonic physics is crucial for advancing precision cluster cosmology studies.

*Acknowledgements.* LM and CG acknowledge the financial contribution from the PRIN-MUR 2022 20227RNLY3 grant ‘The concordance cosmological model: stress-tests with galaxy clusters’ supported by Next Generation EU and from the grant ASI n. 2024-10-HH.0 ‘Attività scientifiche per la missione Euclid – fase E’.

GC thanks the support from INAF theory Grant 2022: Illuminating Dark Matter using Weak Lensing by Cluster Satellites.

GD acknowledges the funding by the European Union - NextGenerationEU, in the framework of the HPC project – ‘National Centre for HPC, Big Data and Quantum Computing’ (PNRR - M4C2 - 11.4 - CN0000013 – CUP J33C22001170001).

SB is supported by the Fondazione ICSC, Spoke 3 Astrophysics and Cosmos Observations. National Recovery and Resilience Plan (Piano Nazionale di Ripresa e Resilienza, PNRR) Project ID CN00000013 ‘Italian Research Center on High-Performance Computing, Big Data and Quantum Computing’ funded by MUR Missione 4 Componente 2 Investimento 1.4: ‘Potenziamento strutture di ricerca e creazione di ‘campioni nazionali di R&S (M4C2-19)’ - Next Generation EU (NGEU); the National Recovery and Resilience Plan (PNRR), Mission 4, Component 2, Investment 1.1, Call for tender No. 1409 published on 14.9.2022 by the Italian Ministry of University and Research (MUR), funded by the European Union – NextGenerationEU – Project Title ‘Space-based cosmology with

Euclid: the role of High-Performance Computing" – CUP J53D23019100001 - Grant Assignment Decree No. 962 adopted on 30/06/2023 by the Italian Ministry of University and Research (MUR).

GC, GD, MM, LM, SB and FM are also supported by the INFN InDark Grant. The authors acknowledge The Red Española de Supercomputación for granting computing time for running most of the simulations of The Three Hundred galaxy cluster project in the Marenostrum supercomputer at the Barcelona Supercomputing Center.

WC and GY would like to thank Ministerio de Ciencia e Innovación for financial support under project grant PID2021-122603NB-C21. WC is also supported by the STFC AGP Grant ST/V000594/1 and the Atracción de Talento Contract no. 2020-T1/TIC-19882 granted by the Comunidad de Madrid in Spain. He also thanks the ERC: HORIZON-TMA-MSCA-SE for supporting the LACEGAL-III project with grant number 101086388 and the China Manned Space Project for its research grants.

## References

- Abbott, T. M. C., Aguena, M., Alarcon, A., et al. 2022, *Phys. Rev. D*, 105, 023520
- Andreon, S. 2010, *MNRAS*, 407, 263
- Andreon, S. 2012, *A&A*, 548, A83
- Andreon, S. 2016, *A&A*, 587, A158
- Andreon, S. & Bergé, J. 2012, *A&A*, 547, A117
- Andreon, S. & Hurn, M. 2013, *Statistical Analysis and Data Mining: The ASA Data Science Journal*, 9, 15
- Arthur, J., Pearce, F. R., Gray, M. E., et al. 2017, *MNRAS*, 464, 2027
- Bahcall, N. A., Fan, X., & Cen, R. 1997, in *American Astronomical Society Meeting Abstracts*, Vol. 190, American Astronomical Society Meeting Abstracts #190, 52.01
- Baltz, E. A., Marshall, P., & Oguri, M. 2009, *J. Cosmology Astropart. Phys.*, 2009, 015
- Bartelmann, M. 2010, *Classical and Quantum Gravity*, 27, 233001
- Bartelmann, M. & Schneider, P. 2001, *Physics Reports*, 340, 291
- Baxter, E. J., Raghunathan, S., Crawford, T. M., et al. 2018, *MNRAS*, 476, 2674
- Beck, A. M., Murante, G., Arth, A., et al. 2016, *MNRAS*, 455, 2110
- Becker, M. R. & Kravtsov, A. V. 2011, *ApJ*, 740, 25
- Bellagamba, F., Roncarelli, M., Maturi, M., & Moscardini, L. 2018, *MNRAS*, 473, 5221
- Bellagamba, F., Sereno, M., Roncarelli, M., et al. 2019, *MNRAS*, 484, 1598
- Benitez-Llambay, A. 2015, *py-sphviewer: Py-SPHViewer v1.0.0*
- Bergamini, P., Acebron, A., Grillo, C., et al. 2023, *ApJ*, 952, 84
- Boldrin, M., Giocoli, C., Meneghetti, M., & Moscardini, L. 2012, *MNRAS*, 427, 3134
- Boldrin, M., Giocoli, C., Meneghetti, M., et al. 2016, *MNRAS*, 457, 2738
- Caminha, G. B., Grillo, C., Rosati, P., et al. 2023, *A&A*, 678, A3
- Carbone, C., Fedeli, C., Moscardini, L., & Cimatti, A. 2012, *J. Cosmology Astropart. Phys.*, 2012, 023
- Chen, M., Cui, W., Fang, W., & Wen, Z. 2024, *ApJ*, 966, 227
- Costanzi, M., Saro, A., Bocquet, S., et al. 2021, *Phys. Rev. D*, 103, 043522
- Costanzi, M., Sartoris, B., Viel, M., & Borgani, S. 2014, *J. Cosmology Astropart. Phys.*, 10, 081
- Cui, W., Dave, R., Knebe, A., et al. 2022, *MNRAS*, 514, 977
- Cui, W., Knebe, A., Yepes, G., et al. 2018, *MNRAS*, 480, 2898
- Cui, W., Power, C., Knebe, A., et al. 2016, *MNRAS*, 458, 4052
- D'Addona, M., Mercurio, A., Rosati, P., et al. 2024, *A&A*, 686, A4
- Davé, R., Anglés-Alcázar, D., Narayanan, D., et al. 2019, *MNRAS*, 486, 2827
- de Jong, J. T. A., Verdoes Kleijn, G. A., Erben, T., et al. 2017, *A&A*, 604, A134
- DESI Collaboration, Adame, A. G., Aguilar, J., et al. 2024, *arXiv e-prints*, arXiv:2404.03002
- Despali, G., Giocoli, C., Angulo, R. E., et al. 2016, *MNRAS*, 456, 2486
- Despali, G. & Vegetti, S. 2017, *MNRAS*, 469, 1997
- Diego, J. M., Li, S. K., Amruth, A., et al. 2024, *A&A*, 689, A167
- Dolag, K., Borgani, S., Murante, G., & Springel, V. 2009, *MNRAS*, 399, 497
- Euclid Collaboration: Blanchard, A., Camera, S., et al. 2020, *A&A*, 642, A191
- Euclid Collaboration: Castro, T., Fumagalli, A., et al. 2022, *arXiv:2208.02174*
- Euclid Collaboration: Giocoli, C., Meneghetti, M., et al. 2024, *A&A*, 681, A67
- Euclid Collaboration: Ingoglia, L., Sereno, M., et al. 2024, *arXiv e-prints*, arXiv:2409.02783
- Euclid Collaboration: Ragagnin, A., Saro, A., Andreon, S., et al. 2024, *arXiv e-prints*, arXiv:2412.00191
- Euclid Collaboration: Sereno, M., Farrens, S., et al. 2024, *A&A*, 689, A252
- Feldbrugge, J. & van de Weygaert, R. 2024, *arXiv e-prints*, arXiv:2405.20475
- Gianfagna, G., Rasia, E., Cui, W., et al. 2023, *MNRAS*, 518, 4238
- Giocoli, C., Marulli, F., Moscardini, L., et al. 2021, *A&A*, 653, A19
- Giocoli, C., Meneghetti, M., Bartelmann, M., Moscardini, L., & Boldrin, M. 2012a, *MNRAS*, 421, 3343
- Giocoli, C., Meneghetti, M., Ettori, S., & Moscardini, L. 2012, *MNRAS*, 426, 1558
- Giocoli, C., Meneghetti, M., Metcalf, R. B., Ettori, S., & Moscardini, L. 2014, *MNRAS*, 440, 1899
- Giocoli, C., Moreno, J., Sheth, R. K., & Tormen, G. 2007, *MNRAS*, 376, 977
- Giocoli, C., Palmucci, L., Lesci, G. F., et al. 2024, *A&A*, 687, A79
- Gnedin, O. Y., Kravtsov, A. V., Klypin, A. A., & Nagai, D. 2004, *ApJ*, 616, 16
- Grandis, S., Bocquet, S., Mohr, J. J., Klein, M., & Dolag, K. 2021, *MNRAS*, 507, 5671
- Grandis, S., Mohr, J. J., Dietrich, J. P., et al. 2019, *MNRAS*, 488, 2041
- Hagger, R., Gray, M. E., Pearce, F. R., et al. 2020, *MNRAS*, 492, 6074
- Hoekstra, H., Hartlap, J., Hilbert, S., & van Uitert, E. 2011, *MNRAS*, 412, 2095
- Hoekstra, H., Yee, H. K. C., & Gladders, M. D. 2004, *ApJ*, 606, 67
- Hoosain, M., Blyth, S.-L., Skelton, R. E., et al. 2024, *MNRAS*, 528, 4139
- Hopkins, P. F. 2015, *MNRAS*, 450, 53
- Ivezic, Z., Tyson, J. A., Abel, B., et al. 2008, *eprint arXiv: 0805.2366* [arXiv:0805.2366]
- Ivezic, Z., Tyson, J. A., Axelrod, T., et al. 2009, in *Bulletin of the American Astronomical Society*, Vol. 41, American Astronomical Society Meeting Abstracts #213, 366
- Jauzac, M., Klein, B., Kneib, J.-P., et al. 2021, *MNRAS*, 508, 1206
- Kilbinger, M. 2015, *Reports on Progress in Physics*, 78, 086901
- Klypin, A., Yepes, G., Gottlöber, S., Prada, F., & Heß, S. 2016, *MNRAS*, 457, 4340
- Knebe, A., Gámez-Marín, M., Pearce, F. R., et al. 2020, *MNRAS*, 495, 3002
- Knollmann, S. R. & Knebe, A. 2009, *ApJS*, 182, 608
- Laureijs, R., Amiaux, J., Arduini, S., et al. 2011, *arXiv:1110.3193*
- Lee, B. E., Le Brun, A. M. C., Haq, M. E., et al. 2018, *MNRAS*, 479, 890
- Lesci, G. F., Marulli, F., Moscardini, L., et al. 2022a, *A&A*, 659, A88
- Lesci, G. F., Nanni, L., Marulli, F., et al. 2022b, *A&A*, 665, A100
- Li, Q., Cui, W., Yang, X., et al. 2023, *MNRAS*, 523, 1228
- Libeskind, N. I., van de Weygaert, R., Cautun, M., et al. 2018, *MNRAS*, 473, 1195
- Lima, M. & Hu, W. 2005, *Phys. Rev. D*, 72, 043006
- Mainieri, V., Anderson, R. I., Brinchmann, J., et al. 2024, *arXiv e-prints*, arXiv:2403.05398
- Malavasi, N., Arnouts, S., Vibert, D., et al. 2017, *MNRAS*, 465, 3817
- Mantz, A. B., Allen, S. W., Morris, R. G., et al. 2016, *MNRAS*, 463, 3582
- Marulli, F., Veropalumbo, A., & Moresco, M. 2016, *Astronomy and Computing*, 14, 35
- Maturi, M., Bellagamba, F., Radovich, M., et al. 2019, *MNRAS*, 485, 498
- McClintock, T., Varga, T. N., Gruen, D., et al. 2019, *MNRAS*, 482, 1352
- Melchior, P., Gruen, D., McClintock, T., et al. 2017, *MNRAS*, 469, 4899
- Meneghetti, M., Argazzi, R., Pace, F., et al. 2007b, *A&A*, 461, 25
- Meneghetti, M., Cui, W., Rasia, E., et al. 2023, *A&A*, 678, L2
- Meneghetti, M., Fedeli, C., Pace, F., Gottlöber, S., & Yepes, G. 2010a, *A&A*, 519, A90
- Meneghetti, M., Melchior, P., Grazian, A., et al. 2008, *A&A*, 482, 403
- Meneghetti, M., Rasia, E., Merten, J., et al. 2010b, *A&A*, 514, A93
- Murata, R., Nishimichi, T., Takada, M., et al. 2018, *ApJ*, 854, 120
- Natarajan, P., Williams, L. L. R., Bradač, M., et al. 2024, *Space Sci. Rev.*, 220, 19
- Navarro, J. F., Frenk, C. S., & White, S. D. M. 1996, *ApJ*, 462, 563
- Navarro, J. F., Frenk, C. S., & White, S. D. M. 1997, *ApJ*, 490, 493
- Oguri, M. & Hamana, T. 2011, *MNRAS*, 414, 1851
- Planck Collaboration. 2016, *Astron. Astrophys.*, 594, A13
- Planck Collaboration, Ade, P. A. R., Aghanim, N., et al. 2014, *A&A*, 571, A20
- Prada, F., Klypin, A. A., Cuesta, A. J., Betancort-Rijo, J. E., & Primack, J. 2012, *MNRAS*, 423, 3018
- Radovich, M., Puddu, E., Bellagamba, F., et al. 2017, *A&A*, 598, A107
- Ragagnin, A., Meneghetti, M., Bassini, L., et al. 2022, *A&A*, 665, A16
- Rasia, E., Borgani, S., Murante, G., et al. 2015, *ApJ*, 813, L17
- Rozo, E., Rykoff, E. S., Becker, M., Reddick, R. M., & Wechsler, R. H. 2015, *MNRAS*, 453, 38
- Rykoff, E. S., Rozo, E., Busha, M. T., et al. 2014, *ApJ*, 785, 104
- Rykoff, E. S., Rozo, E., Hollowood, D., et al. 2016, *ApJS*, 224, 1
- Santiago-Bautista, I., Caretta, C. A., Bravo-Alfaro, H., Pointecouteau, E., & Andernach, H. 2020, *A&A*, 637, A31
- Saro, A., Bocquet, S., Rozo, E., et al. 2015, *MNRAS*, 454, 2305
- Sartoris, B., Biviano, A., Fedeli, C., et al. 2016, *MNRAS*, 459, 1764
- Sartoris, B., Borgani, S., Fedeli, C., et al. 2010, *MNRAS*, 407, 2339
- Sheth, R. K. & Tormen, G. 1999, *MNRAS*, 308, 119
- Simet, M., McClintock, T., Mandelbaum, R., et al. 2017, *MNRAS*, 466, 3103
- Springel, V., White, S. D. M., Tormen, G., & Kauffmann, G. 2001, *MNRAS*, 328, 726
- Srivastava, A., Cui, W., Meneghetti, M., et al. 2024, *MNRAS*, 528, 4451
- Tinker, J., Kravtsov, A. V., Klypin, A., et al. 2008, *ApJ*, 688, 709
- Tormen, G. 1998, *MNRAS*, 297, 648
- Tormen, G., Diaferio, A., & Syer, D. 1998, *MNRAS*, 299, 728
- Tormen, G., Moscardini, L., & Yoshida, N. 2004, *MNRAS*, 350, 1397
- van den Bosch, F. C. 2002, *MNRAS*, 331, 98
- Vega-Ferrero, J., Dana, J. M., Diego, J. M., et al. 2021, *MNRAS*, 500, 247
- von der Linden, A., Allen, M. T., Applegate, D. E., et al. 2014, *MNRAS*, 439, 2
- Wang, Y., Pearce, F., Knebe, A., et al. 2018, *ApJ*, 868, 130
- Wechsler, R. H., Bullock, J. S., Primack, J. R., Kravtsov, A. V., & Dekel, A. 2002, *ApJ*, 568, 52
- Zhang, Y., Guo, H., Yang, X., & Wang, P. 2024, *MNRAS*, 533, 1048